Atmosphere circulation patterns synchronize pan-Arctic glacier melt and permafrost thaw

Check for updates

Ingo Sasgen [1,2] ✉, Grit Steinhoefel[3], Caroline Kasprzyk[1,4], Heidrun Matthes [5], Sebastian Westermann[6], Julia Boike [7,8] & Guido Grosse [7,9]

The Arctic is changing rapidly due to the amplification of global temperature trends, causing profound impacts on the ice sheet in Greenland, glaciers, frozen ground, ecosystems, and societies. Here, we focus on impacts that atmospheric circulation causes in addition to the climate warming trends. We combine time series of glacier mass balance from temporal satellite gravimetry measurements (GRACE/GRACE-FO; 2002–2023), active layer thickness in permafrost areas from ESA's Climate Change Initiative remote sensing and modelling product (2003–2019), and field measurements of the Circumpolar Active Layer Monitoring Network (2002–2023). Despite regional and system-related complexities, we identify robust covariations between these observations, which vary asynchronously between neighbouring regions and synchronously in regions antipodal to the North Pole. We reveal a close connection with dominant modes of atmosphere circulation, controlling about 75% of the common pan-Arctic impact variability (2002–2022), also affecting the Greenland Ice Sheet. We emphasize that it is necessary to consider such atmospheric driving patterns when projecting impacts, particularly caused by extremes, in an increasingly warmer Arctic.

The Arctic is experiencing profound transitions due to climate change[1]. From 1979 to 2021, summer temperatures in the Arctic were rising twice as fast as the global average, with annual mean temperatures increasing close to four times faster[2] due to Arctic amplification[3–5]. This warming leads to various environmental changes[6–8] such as glacier mass loss[9], permafrost warming, thaw and degradation[10–12], reduced snow cover extent[13] and decreasing summer sea ice extent[14]. For individual years, impacts are often modified by the superposition of these long-term regional warming trends with synoptic atmosphere conditions[2].

The consequences of these transitions extend globally, and include sea-level rise from the Arctic glacier systems[15] and the Greenland Ice Sheet[16], modification of teleconnections through reduced snow cover and sea ice extent[17], and carbon and methane release from permafrost regions[18], with impacts on ecosystems and societies[1]. Even if temperatures stabilize, glacier mass loss is projected to persist for decades to centuries[19], together with a continued warming and thawing of thick permafrost (tens to hundreds of meters)[20]. To date, the positive feedback of global warming with the release of greenhouse gases due to permafrost thaw and associated degradation of organic matter remains poorly represented in climate models, making projections even more uncertain[21,22].

Since the late 1990s[23], glaciers in the Arctic have continuously been losing mass with Alaska, Arctic Canada, Svalbard, and the Russian Arctic together contributing each year about 0.39 ± 0.05 mm (mass change of -140.4 ± 18.0 Gt) to sea level rise between 2003–2016[15]. Increasing Arctic temperatures have enhanced the summer melt production of glaciers, outweighing any regional counterbalance by snow accumulation[6].

Furthermore, increasing temperatures strongly promote degradation of permafrost. Permafrost is defined as ground that remains at or below 0 °C

[1]Division of Geosciences, Glaciology Section, Alfred-Wegener-Institut Helmholtz-Zentrum für Polar- und Meeresforschung, Am Handelshafen 12, 27570 Bremerhaven, Germany. [2]Institute of Geography, University of Augsburg, Alter Postweg 118, 86159 Augsburg, Germany. [3]Divisions of Biosciences and Geosciences, Marine Biogeosciences and Marine Geochemistry Sections, Alfred-Wegener-Institut Helmholtz-Zentrum für Polar- und Meeresforschung, Am Handelshafen 12, 27570 Bremerhaven, Germany. [4]Institute for Geology, Mineralogy and Geophysics, Ruhr-Universität Bochum, 44780 Bochum, Germany. [5]Division of Climate Sciences, Atmospheric Physics Section, Alfred-Wegener-Institut Helmholtz-Zentrum für Polar- und Meeresforschung, Telegrafenberg A45, 14473 Potsdam, Germany. [6]Department of Geosciences, Section of Physical geography and Hydrology, University of Oslo, Postboks 1047 Blindern, 0316 Oslo, Norway. [7]Division of Geosciences, Permafrost Research Section, Alfred-Wegener-Institut Helmholtz-Zentrum für Polar- und Meeresforschung, Telegrafenberg A45, 14473 Potsdam, Germany. [8]Geography Department, Humboldt-Universität zu Berlin, Unter den Linden 6, 10099 Berlin, Germany. [9]Institute of Geosciences, University of Potsdam, Karl-Liebknecht-Str. 24-25, 14476 Potsdam, Germany. ✉e-mail: ingo.sasgen@awi.de

for at least two consecutive years[24]. In the Arctic, the continuous permafrost zone (> 90% of the land surface is underlain by permafrost) is estimated to cover 41% of the land-based regions north of 60°N[25], and experienced mean annual ground temperature increase of 0.39 ± 0.15 °C between 2007 and 2016[10]. Despite some regional differences, an overall warming trend has been observed since the mid-1980s with record highs in permafrost temperature at the majority of the observation sites in 2019[11,12]. The uppermost soil layer above the permafrost that thaws and refreezes seasonally is called the active layer[26]. As a result of increasing ground temperatures and an increase in the active layer thickness, permafrost is retreating laterally and vertically in many regions[27–29]. Annual mean frozen volume in permafrost areas are projected to decrease by 10–40% per °C warming of global mean surface-air temperature for the uppermost two meters[30].

Atmospheric circulation patterns that enhance the transport of heat to the Arctic have become more frequent since 2000[31,32], enabling regional record values of glacier mass loss and permafrost temperatures[11,33,34]. Even though understanding the impacts of dynamic changes in atmospheric circulation is crucial, it poses a significant challenge to disentangle natural variability from that caused by anthropogenic climate change[5,35]. This complexity is particularly evident when examining trends in the frequency of Greenland blocking conditions, reflected by the Greenland Blocking Index (GBI)[36], which surpass the predictions made by hindcast simulations of the Climate Model Intercomparison Project (CMIP6)[37].

Here, we advance with understanding the impacts of atmosphere variability on glacier and permafrost systems in the Arctic using satellite, remote sensing, modelling and in situ data (Fig. 1). We focus on terrestrial systems (glaciers and permafrost) with their high sensitivity to summer atmosphere conditions and subsume their covariations in an index reflecting pan-Arctic variability. Observations connected to ocean processes, like minimum summer sea ice extent or sea surface temperature, are not included, because of their indirect and more complex relation to summer atmosphere conditions[38]. The data set we use consists of a diverse set of observations, namely, glacier mass change from the Gravity Recovery and Climate Experiment (GRACE) and its follow-on GRACE-FO (2002–2023) satellite gravimetry missions, as well as active layer thickness from the

European Space Agency (ESA) Climate Change Initiative (CCI) Permafrost product (2003–2019) based on satellite remote sensing and modelling, and the Circumpolar Active Layer Monitoring Network (CALM) in situ field observation network (2002–2023), available since the 1990s[39]. Using reanalysis data, we resolve the main modes of atmosphere circulation over the Arctic, and demonstrate their relevance for driving pan-Arctic impacts.

Results

Trends in glacier mass and active layer thickness
First, we present temporal change in glacier mass and active layer thickness across the Arctic, and estimate related linear trends (Fig. 2). We utilized data from the GRACE/GRACE-FO missions, which employ an intra-satellite link to detect subtle variations in Earth's gravity field caused by mass redistributions at spatial scales of 300 km with an accuracy of 2 cm water equivalent[40,41]. Our analysis of the GRACE/GRACE-FO data revealed ongoing mass loss in all Arctic glacier systems between 2002 and 2023, aligning with rising Arctic temperatures.

Integrated over each glacier region (Fig. 1a), the largest rate of mass change observed by GRACE/GRACE-FO (Fig. 2a–h) originated from the Gulf of Alaska (ALGO), amounting to -46.5 ± 13.4 Gt yr^{-1} ($\pm 2\sigma$), followed by Northern Arctic Canada (CANN) with -29.9 ± 5.6 Gt yr^{-1} (Fig. 2c), and Svalbard (SVAL) with -14.8 ± 1.3 Gt yr^{-1} (Fig. 2e). We observed less negative, yet statistically significant, rates of mass change in the range of -9 to -2 Gt yr^{-1} for the islands in the Russian Arctic (FJRO, NOZE and SEZE, Fig. 2f–h). For the rate of specific mass change – the rate of mass change divided by the glacier area[15,42], expressed in terms of equivalent water height change, the largest value is observed for ALGO (-0.66 ± 0.19 m yr^{-1}) and SVAL (-0.43 ± 0.04 m yr^{-1}). The remaining glacier systems also show significant trends between -0.38 and -0.16 m yr^{-1} with an uncertainty of typically ± 0.05 m yr^{-1}. Exceptions are ALNO with -0.25 ± 0.90 m yr^{-1} and CANS with -0.28 ± 0.27 m yr^{-1} (no significance), where uncertainties in the trends are caused by the comparably large spread of glacial-isostatic adjustment corrections of the GRACE/GRACE-FO data (Methods).
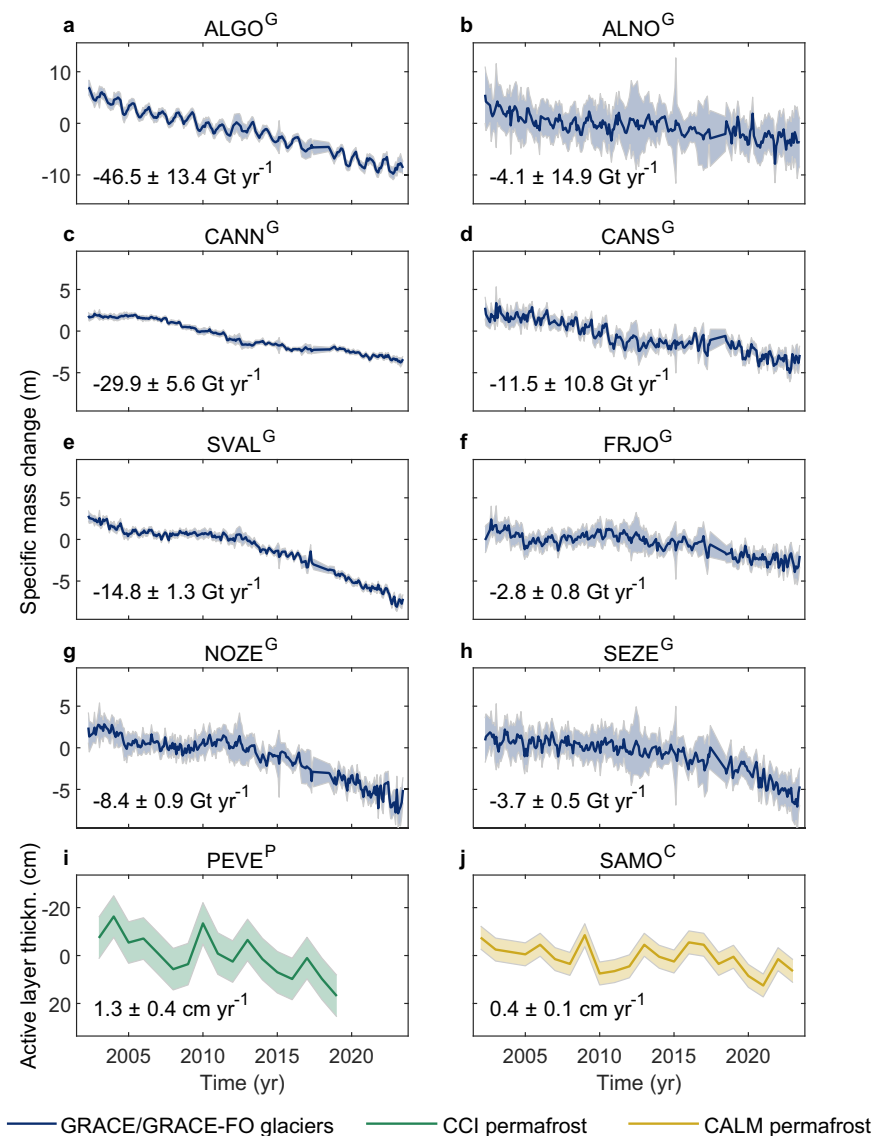
Our estimates of changes in active layer thickness are based on two data sources; field measurements at stations within the CALM network
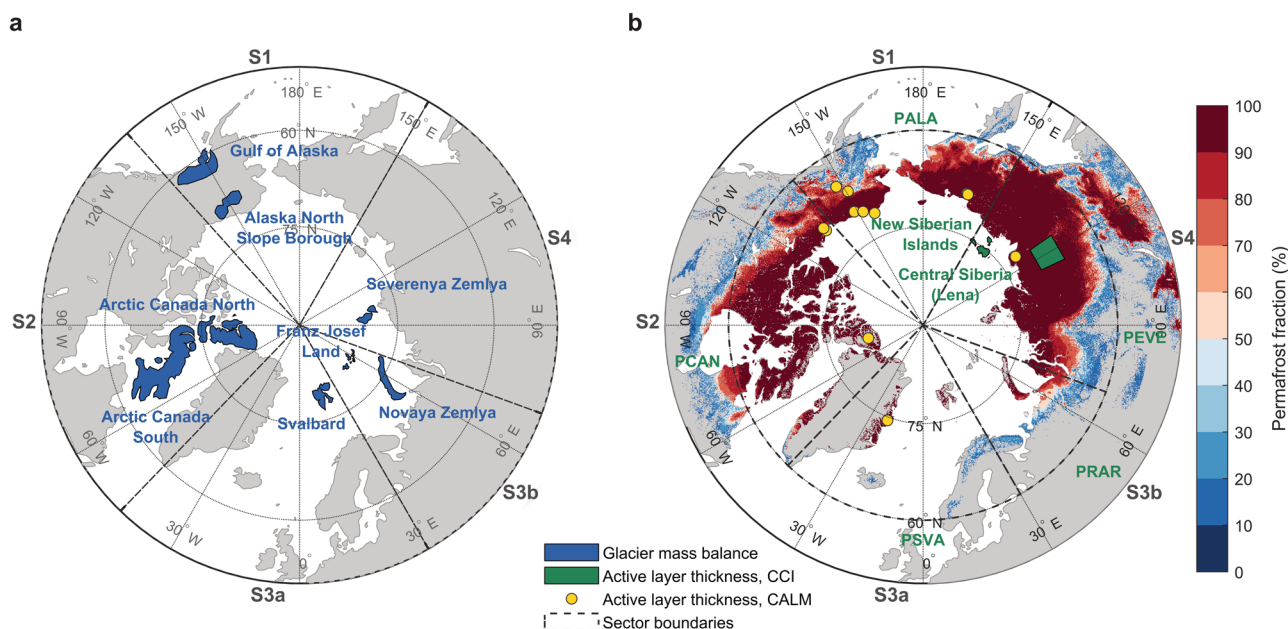
Fig. 1 | Glacier and permafrost regions in the Arctic. a Glacier systems in the Arctic with mass balance estimates from GRACE/GRACE-FO (blue); Gulf of Alaska (ALGO), Alaska North Slope Borough (ALNO), Arctic Canada North (CANN; >74°N), Arctic Canada South (CANS < 74°N), Franz Josef Land (FRJO), Novaya Zemlya (NOZE), Severnaya Zemlya (SEZE) and Svalbard (SVAL). **b** Permafrost fraction, as well as locations of active layer thickness estimates at selected CALM sites (yellow circles), and within the regions of New Siberian Islands (SIBI) and Lena, Central Siberia (LENA) based on CCI data (green). Dashed lines indicate the longitudes delineating the sectorial averages of the CCI data north of 60°N; Alaska (PALA; S1), Northern Canada (PCAN; S2), Svalbard (PSVAL; S3a), the European Russian Arctic (PRAR; S3b) and Western and Central Siberia (PEVE; S4).

Fig. 2 | Time series of changes in glacier mass and active layer thickness. a–h Monthly mass change of the Arctic glacier systems from GRACE/GRACE-FO satellite gravimetry data for the time period 2002–2023 (blue), annual change of the mean active layer thickness from CCI permafrost data (2003–2019) for the region PEVE (green) (**i**) and at CALM station Samoylov (SAMO) for 2002–2023 (yellow) (**j**) as departure from the long-term mean. Uncertainties are shown as two standard deviations (± 2σ; shading). The respective rates of glacier mass change (Gt yr⁻¹) and rates of active layer thickness change (cm yr⁻¹) for each region are indicated along with ± 2σ uncertainties in panels **a–j**. Changes are shown with respect to the 2003–2019 mean.

For all permafrost regions shown in Fig. 1b, average increases in active layer thickness are in the range of 0.4 to 1.4 cm yr⁻¹ based on the CCI data. For example, the PEVE sector of Siberia, Russia (Fig. 1) exhibited a significant long-term trend in active layer thickness increase of 1.3 ± 0.5 cm yr⁻¹ (2003–2019) (Fig. 2j), resulting in an increase of 20 cm between 2003 and 2019. Similarly, yet a weaker trend of 0.4 ± 0.1 cm yr⁻¹ (2003–2019) is measured at the CALM field station Samoylov (SAMO), located within the Lena Delta, Siberia, Russia[39,45] (Fig. 2i), PEVE sector in Fig. 1. Station SAMO is selected here as an example for a station with a time series that is consistent with the CCI data at interannual time scales (Supplementary Fig. 1). But many in situ measurements show varying trends in active layer thickness depending on the local geomorphology, microclimate and environmental conditions, which are not captured by the CCI data[11,20].

Covariation of glacier and permafrost systems between regions

In the following, we focus on interannual (detrended) annual changes of glacier mass and active layer thickness (Methods). Correlation between

(2002–2023)[39,43] derived from the end-of-season thaw depth or temperature measurements in boreholes, and regional and sectorial averages based on ESA's CCI permafrost data set for 2003–2019, which combines modelling with satellite remote sensing data[25,44] (Methods). Regional changes in active layer thickness based on CALM network data were also presented in ref. 20 and are regularly assessed in the State of Climate reports[11].

GRACE/GRACE-FO mass changes of each glacier system and the active layer thickness from the CCI data reveal strikingly similar patterns at interannual time scales (Fig. 3). Interestingly, active layer thickness and glacier mass change do not only covary in proximity, but typically also show correlation patterns antipodal with respect to the North Pole. For example, annual glacier mass balances in Northern Arctic Canada (CANN) show negative correlation with the changes in active layer thickness across the Arctic, in central Siberia (Fig. 3c). This means that for example cold conditions contributing to a higher glacier mass balance (weaker mass loss) in CANN are associated with a lower active layer thickness (shallower thaw depth) in central Siberia, and vice versa. Remarkably, glaciers in the North Atlantic and European Russian Arctic (SVAL, FRJO, NOZE) exhibit correlation of opposite sign with the active layer thickness in Northern Arctic Canada and central Siberia (Fig. 3e–g), suggesting a common, yet regionally distinct driver of impacts across most of the Arctic.

To systematically uncover the covariations between systems and regions in the Arctic, we conduct a factor analysis, which is a statistical method to estimate how closely observations are related to (load onto) a common temporal behaviour (factor) (Methods). We use time series of standardized anomalies of GRACE/GRACE-FO annual mass balances of eight glacier regions, as well as seven CCI estimates of active layer thickness changes; two averages for the New Siberian Islands (SIBI) and the Lena River Delta, Siberia (LENA), as well as five sectorial averages (PALA, PCAN,
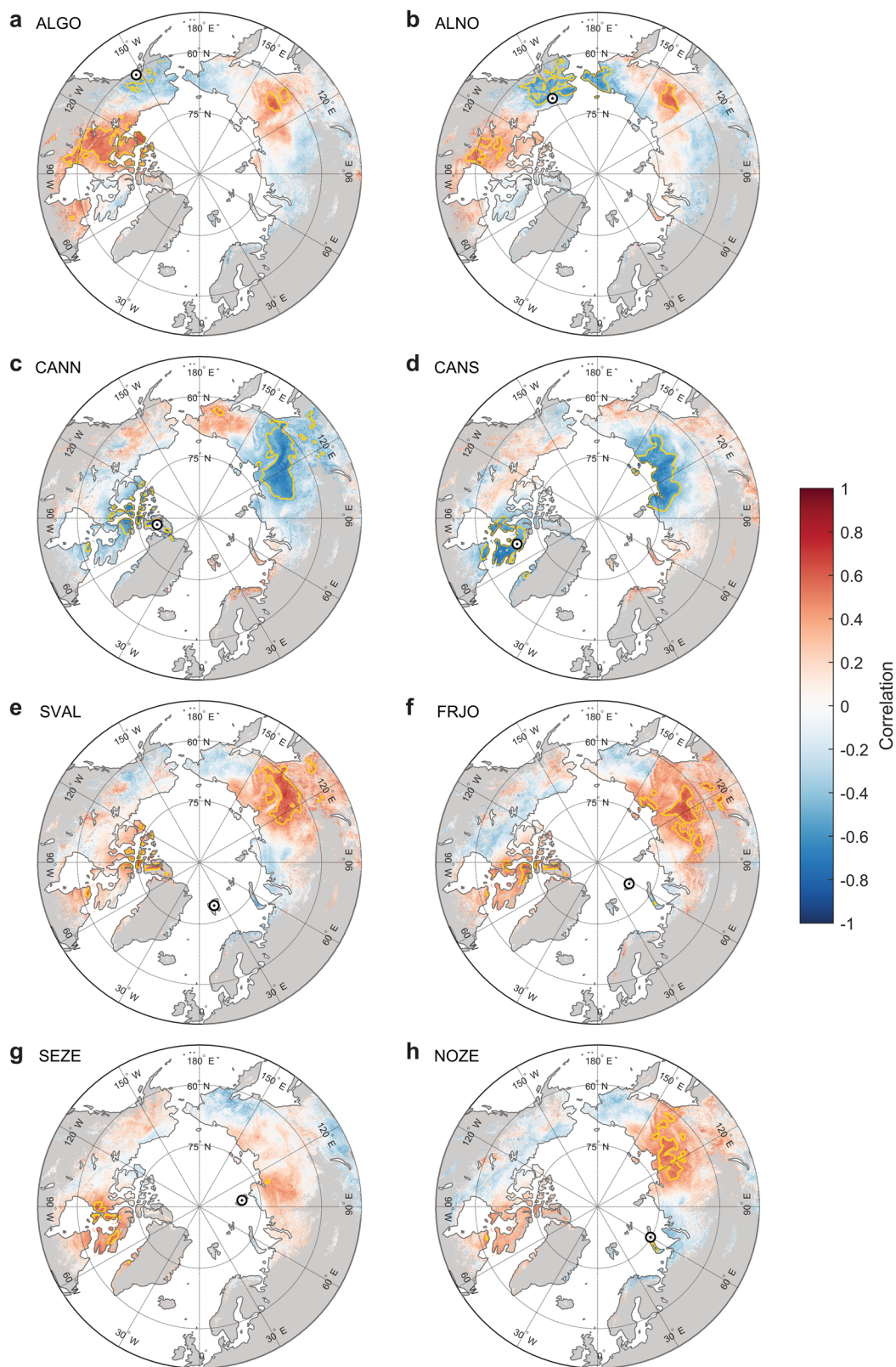
Fig. 3 | Correlation of glacier mass balance and active layer thickness in Artic permafrost regions. Correlation (lag zero) of the annual glacier mass balances from GRACE/GRACE-FO satellite gravimetry data with the mean active layer thickness from CCI permafrost data for the 2003–2019. Following our definition of the anomalies, glacier mass balance and active layer thickness in proximity are expected to be anti-correlated meaning that glacier mass gain correspond to low active layer thickness. The mean geographical coordinate of the glacier system is shown as circle for, **a** ALNO, **b** ALGO, **c** CANN, **d** CANS, **e** SVAL, **f** FRJO, **g** NOZE and **h**, SEZE. Areas of significance (*p*-value < 0.05), accounting for autocorrelation in both the GRACE/GRACE-FO and CCI data, are indicated by yellow dotted contours.
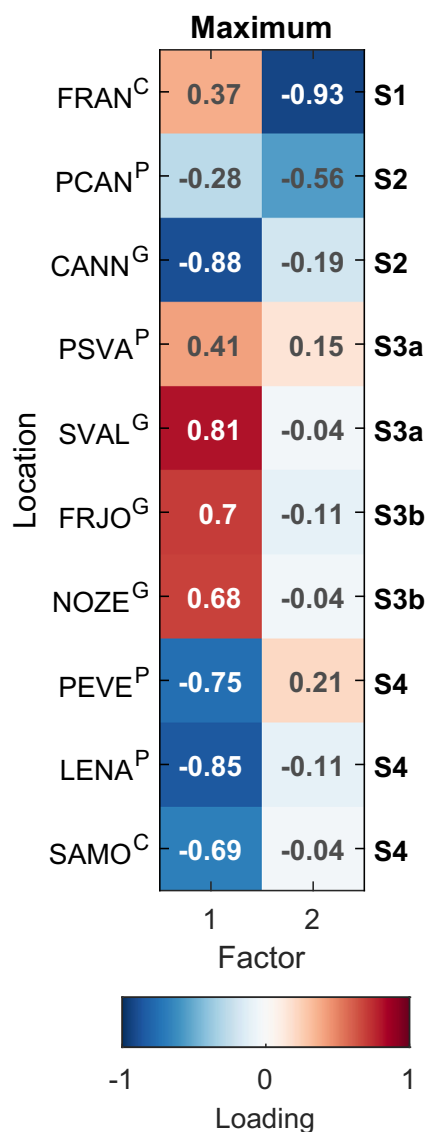
Fig. 4 | Factor analysis of changes in glacier mass and active layer thickness. Shown are factor loadings for the ensemble member with the maximum total factor loading. Superscripts indicate the data type associated with each location, namely glacier (G), CCI permafrost (P) – regional or sectorial averages, and CALM station permafrost data (C), their associated sector is indicated on the right axis (S1, S2, S3a/b, and S4). The first factor carries the largest load and is selected for further investigation.

PSVAL, PRAR and PEVE) (Fig. 1 and Supplementary Fig. 2). The sectors broadly reflect the areas of covariation shown in Fig. 3. To expand the data sets, we include 13 field measurements of the active layer thickness from the long-term permafrost monitoring network CALM[43,46,47]. Criteria to select these 13 sites among 185 available measurements north of 60°N are that they provide nearly continuous time series for 2003–2019 (one missing year allows), are not co-located with highly correlated time series, and show significant correlation in terms of interannual variations with CCI data (Methods and Supplementary Fig. 1). Our methodology builds upon that of Overland et al. [48] in which factor analysis was applied to a diverse set of Arctic climate variables that included long-term trends; here we focus entirely on interannual changes.

In an ensemble approach ($N \approx 140000$), we randomly selected ten observations from the pool of 28 standardized time series, while ensuring that each ensemble member contained at least one location from each of the five sectors shown in Fig. 1 to guarantee pan-Arctic sampling (Method). We find that the factor analysis indicates the highest sum of significant factor

loadings (closest relation) for the set of four glacier mass balances CANN, SVAL, FRJO, and NOZE, as well as the active layer thickness for the regional and sectorial averages LENA and PEVE, respectively, and the field measurement SAMO (Fig. 4). Negative factor loadings were carried by observations from sectors S2 (Northern Canada) and S4 (Western and Central Siberia), while positive factor loadings originated from sectors S3a (North Atlantic) and S3b (European Russian Arctic). We highlight that factor loadings of opposite sign reflect asynchronous temporal behaviour. Therefore, the factor analysis confirms the large-scale division of the correlation patterns shown in Fig. 3. Most of the time, observations from the Alaska and Bering Strait area (sector S1) load onto Factor 2 indicating a temporal behaviour distinct from that reflected by Factor 1.

Temporal signature of the glacier and permafrost impacts
Next, we derived two types of indices, called the Arctic Impact Indices, to capture the pan-Arctic covariations (Fig. 5). The first index, $AIIn_F$, is based on the factor analysis itself. It represents the ensemble mean of the Factor 1 time series of 98 ensemble members selected based on their significance (Methods). This index requires continuous data and therefore covers only the time period 2003–2019, limited by the availability of continuous CCI data of active layer thickness.

The second index, $AIIn_S$, is based on the time series for each location directly. The locations are chosen due to their dominantly high and significant loadings in the factor analysis, regardless of the ensemble composition. The index $AIIn_S$ was then derived as double-standardized differences of the covarying blocks (positive or negative) of observations. This index does not require continuous input data, which allowed us to extend the time series to the full length of GRACE/GRACE-FO annual mass balances (2002–2022). For both types of indices, we estimated the mean and standard deviation of the ensemble, to assess their sensitivity to the selected input data. For $AIIn_S$, we additionally propagated uncertainties in the input data sets to the index and added them to the ensemble spread (Methods).

Both, $AIIn_F$ and $AIIn_S$, exhibited very similar variations over time (Fig. 5a), with marked positive values in 2004, 2013, and 2017, and pronounced negative values in 2008, 2011, and 2012. In addition, indices based on the ensemble maximum and the ensemble mean showed only minor differences (Fig. 5a). Note that we define the indices such that positive values correspond to positive anomalies in glacier mass balance (less mass loss) in Northern Arctic Canada (CANN) and reduced active layer thickness (shallower thaw depth) in covarying central parts of Siberia (LENA).

Seven observations stood out as contributing most to the indices (Fig. 5b); glacier mass changes of FRJO, NOZE, and SVAL (positive) and CANN (negative), as well as active layer thickness of the regional average LENA, the sectorial average PEVE, and this in situ measurement SAMO (all negative). Of the 13 field measurements at the CALM stations available in the pool of observations, only Samoylov (SAMO) consistently carried a significant factor load. The glacier mass balance at CANS and active layer thickness at SIBI sometimes contributed significantly to the indices, depending on overall ensemble composition (Fig. 5b). If the ensemble contained an observation from the European Russian Arctic (S3b) or the North Atlantic (S2) they were likely contributed to the indices (90% and 77% of the time, respectively). Observations from Northern Canada (S2) contributed 49% of the time, while data drawn from the sector including Alaska (S1) never carried significant loads (Fig. 5c).

Pan-Arctic impacts from atmospheric drivers
Next, we investigated the atmospheric drivers of glacier mass balance and active layer thickness anomalies, as reflected by the indices. Specifically, we focused on the summer months (June, July and August or JJA), which dominantly control glacier mass balance through summer meltwater runoff[49] and the annual maximum active layer thickness[50] typically taken at the end of August and mostly well into September[51] as a result of integrated summer temperatures. It should be noted that the connection between summer air temperature and active layer thickness is less pronounced where there is a thick buffer layer (for example, an organic layer) or high ground ice
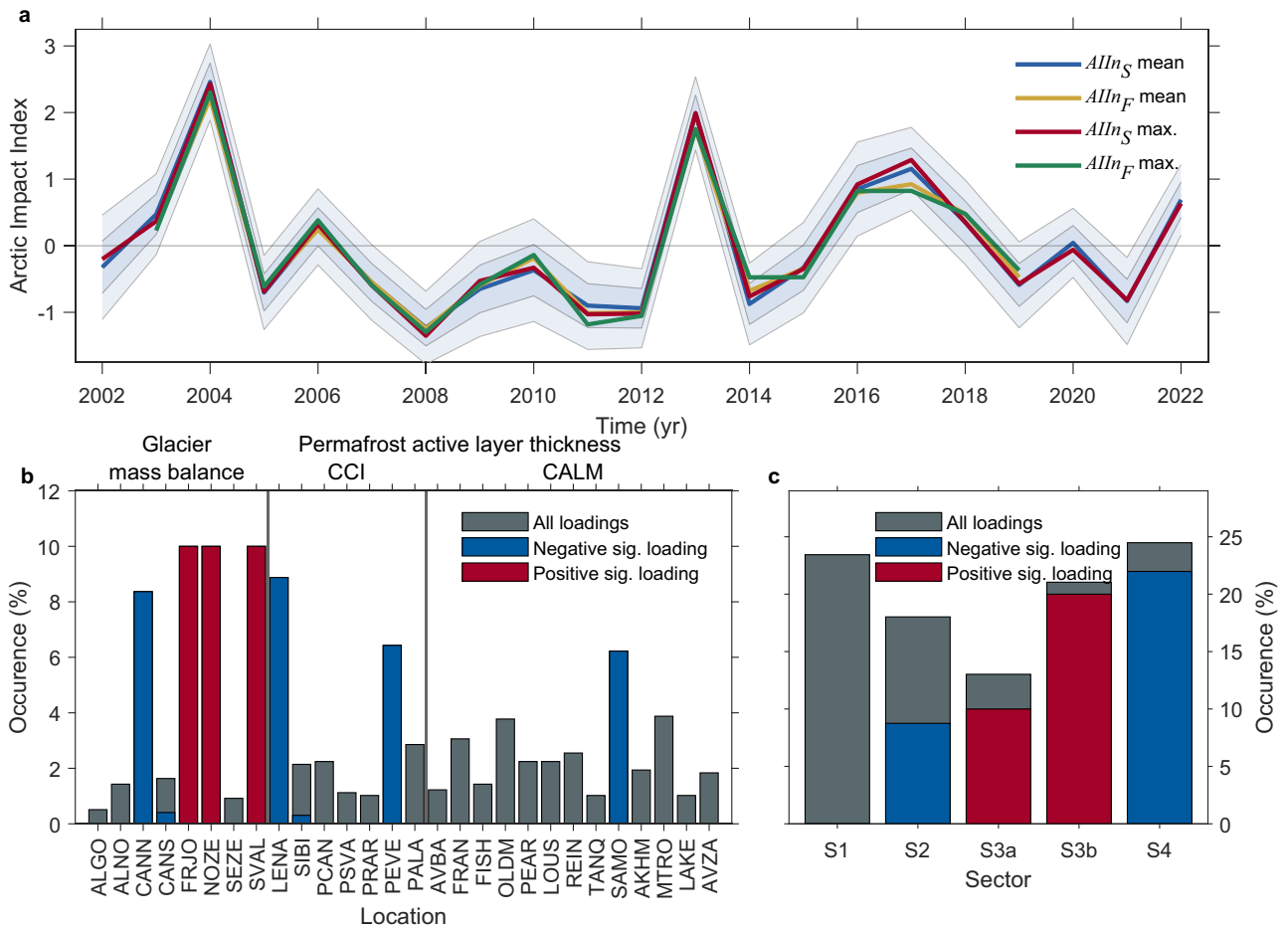
Fig. 5 | Time series and location composition of Arctic Impact Indices. a Time series of the Arctic Impact Indices based on the ensemble mean and maximum of the factor loadings for 2003–2019, $AIIn_F$, as well as based on the differences of observations with significant loading for 2002–2022, $AIIn_S$. Uncertainties are shown for the mean $AIIn_S$ as one standard deviation (±1σ; dark grey) and two standard deviations (±2σ; light grey). **b** Overall, random occurrence of each of the 28 observations in all ensemble members exceeding the significance threshold (grey) and additionally carrying a significant positive (red) and negative (blue) load, as well as their observation type (top). **c** Sector attribution of all locations (grey) and those with significant positive (red) and negative (blue) loadings as shown in **b**.

content[20]. To this end, we analysed two key atmospheric variables indicative of large-scale summer circulation patterns based on monthly re-analysis data of National Center for Environmental Prediction (NCEP)/National Center for Atmospheric Research (NCAR)[52]: the geopotential height of the 500 hPa pressure surface (z500) and the air temperature at the 700 hPa level (t700).

The correlations of 500 hPa geopotential height (z500) and 700 hPa temperature (t700) with the Arctic Impact Indices $AIIn_F$ (2003–2019) and $AIIn_S$ (2002–2022) are shown in Fig. 6. Regardless of index type, z500 consistently exhibited patterns of positive correlation over central North America, the European Russian Arctic, Western and Central Siberia, with negative correlation over Greenland stretching over the North Pole towards Eastern Siberia. Negative correlations imply that a positive index value, representing less mass loss in CANN and shallower active layer thickness in SAMO, as in 2004, corresponds to negative geopotential height anomalies, favouring cold conditions in these regions. The correlations of the indices with t700 reveals a strong regional control of the impacts by air temperature variations (Fig. 6). Both atmospheric variables displayed bimodal correlation patterns with the indices that extended across the Arctic, remarkably independent of the underlying time periods 2002–2022 (Fig. 6a, c) and 2003–2019 (Fig. 6b, d).

Relation to summer atmosphere variability in the Arctic
Next, we freely decompose atmosphere variability in the Arctic to investigate the connection to the impacts reflected by the indices. We find the main modes contained in the time series of atmospheric fields of z500 for time

periods 2002–2022 ($AIIn_S$) and 2003–2019 ($AIIn_F$), respectively, using Empirical Orthogonal Functions (EOFs) (Methods). By regressing the indices onto the independently determined EOFs principal components (PCs), we identify the modes most relevant for inducing the estimated covariation among the Arctic impacts (Fig. 7).

Both indices exhibited a high correlation ($r \cong 0.6$; $p<0.01$) with the dominant mode of atmosphere variability reflected by PC1/EOF1, which accounts for 28% of the total variability in z500. Figure 7c, d show that the PC1/EOF1 pattern is characterized by opposing pressure changes over the Arctic Ocean and more southern latitudes, extending southward over Greenland to around 50°N. The pattern encompasses regions of the North Atlantic Oscillation (NAO) (Iceland and Western Europe), as well as of the larger Greenland area used to define the GBI – two indices known to anti-correlate[36]. This suggests that EOF1/PC1 reflects a superposition of NAO- and GBI-related circulation patterns, which is further supported by a significant corelation with NAO ($r = 0.8$) and anti-correlation with the GBI ($r = −0.8$) (Fig. 7a, b).

However, we identified a second EOF mode correlating significantly ($p<0.03$) with both Arctic indices (Fig. 7e, f), but not with the NAO and GBI. The spatial pattern of this mode is more complex than that of EOF1; it is characterized by four regions of strong variability for $AIIn_S$, up to at most six for $AIIn_F$. This pattern explains approximately 8–9% of the total variability in z500. Together, these two EOF modes account for 36–37% of the variability in the atmosphere, but they specifically explained 74% and 83% common variability Arctic impacts subsumed in $AIIn_S$ and $AIIn_F$, respectively (Fig. 7a, b).
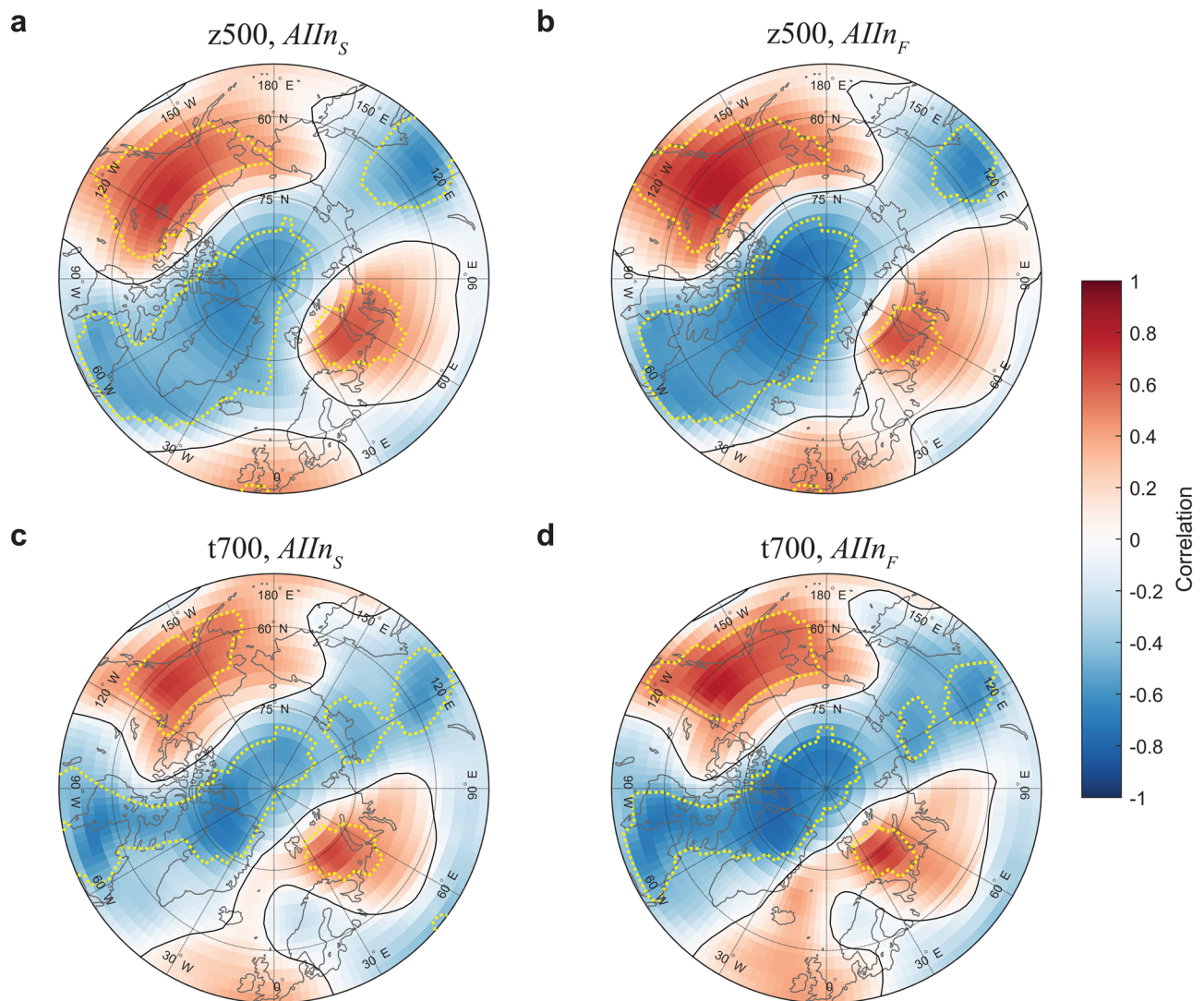
Fig. 6 | Correlation of Arctic Impact Indices with atmospheric variables. Correlation (lag zero) of the detrended summer (JJA) mean of the 500 hPa geopotential height with **a,** $AIIn_S$ for the time period 2002–2022, and **b,** $AIIn_F$ for the time period 2003–2019. Areas of significance (p-value < 0.05), accounting for autocorrelation in both the atmosphere data and indices, are indicated by yellow dotted contours. **c, d** are analogue to **a, b,** but show correlations of the indices with detrended summer mean of the temperature at the 700 hPa geopotential height.

Discussion

We have focused on the direct (lag zero) impact of summer atmospheric circulation patterns on glacier mass balance and active layer thickness. Several preconditioning factors are known to affect the summer response of the glacier[53,54] and permafrost systems[55]; for example, early snowmelt promotes glacier melting, or a thick snow cover in autumn hinders deep freezing early in winter, affecting the active layer thickness in summer[56]. Winter warming events have gained relevance in the pre-conditioning the shallow ground thermal regime[20,57]. However, for the time period 2002–2022, despite such complexities, we find significant temporal correlations of changes in glacier mass in Northern Canada, the North Atlantic and European Russian Arctic and active layer thickness in central parts of Siberia, synchronous between regions antipodal to the North Pole, and asynchronous for neighboring regions (Fig. 8).

For the time period 2003–2019, shared variations reflected in $AIIn_F$ explain the variance of interannual annual mass changes of four Arctic glaciers systems by more than 46% (CANN, FRJO, NOZE and SVAL), as well as with active layer thickness changes by more than 81% for the Lena Delta (LENA) (Fig. 8). In 26% of the area of Western and Central Siberia (PEVE) the index significantly reduces the variance. Furthermore, the indices represented more than 51% of the variance in the field measurements of active layer thickness at

Samoylov station (SAMO). For Northern Canada, significant correlation of the index and active layer thickness is observed for 10% of the sectorial area, mainly covering the northeastern Canadian Arctic Archipelago (Fig. 8). Lower correlation values, however, below the significance level, were obtained for CANS (49%; explained variance 24%). Also, Severnaya Zemlya (SEZE) fell below the significance level, likely due to a weak signal difficult to resolve in the presence of noise in GRACE/GRACE-FO data. The regions of Alaska (ALGO and ALNO) do not significantly covary with the indices, pointing to an additional influence of other atmospheric circulation patterns, related, for example, to the Pacific Decadal Oscillation, El Niño Southern Oscillation, or atmospheric blocking over Alaska[58], known to also influence northwestern Canada[59].

We find that interannual variability of mass changes of northern Greenland, which are not contributing to the indices, correlate strongly with CANN, enabling a representation by the index by over 50% (explained variance) for the drainage basins north of about 72°N (2003–2019) (Fig. 8). Southwestern Greenland shows similar values of correlation with the index as the proximal CANS (about 50%), also synchronous with northern Greenland, but without statistical significance. The reason for the covariation is that atmospheric blocking, linked to the GBI (part of EOF1 mode), has been responsible for recent extreme surface melt by the delivery of heat
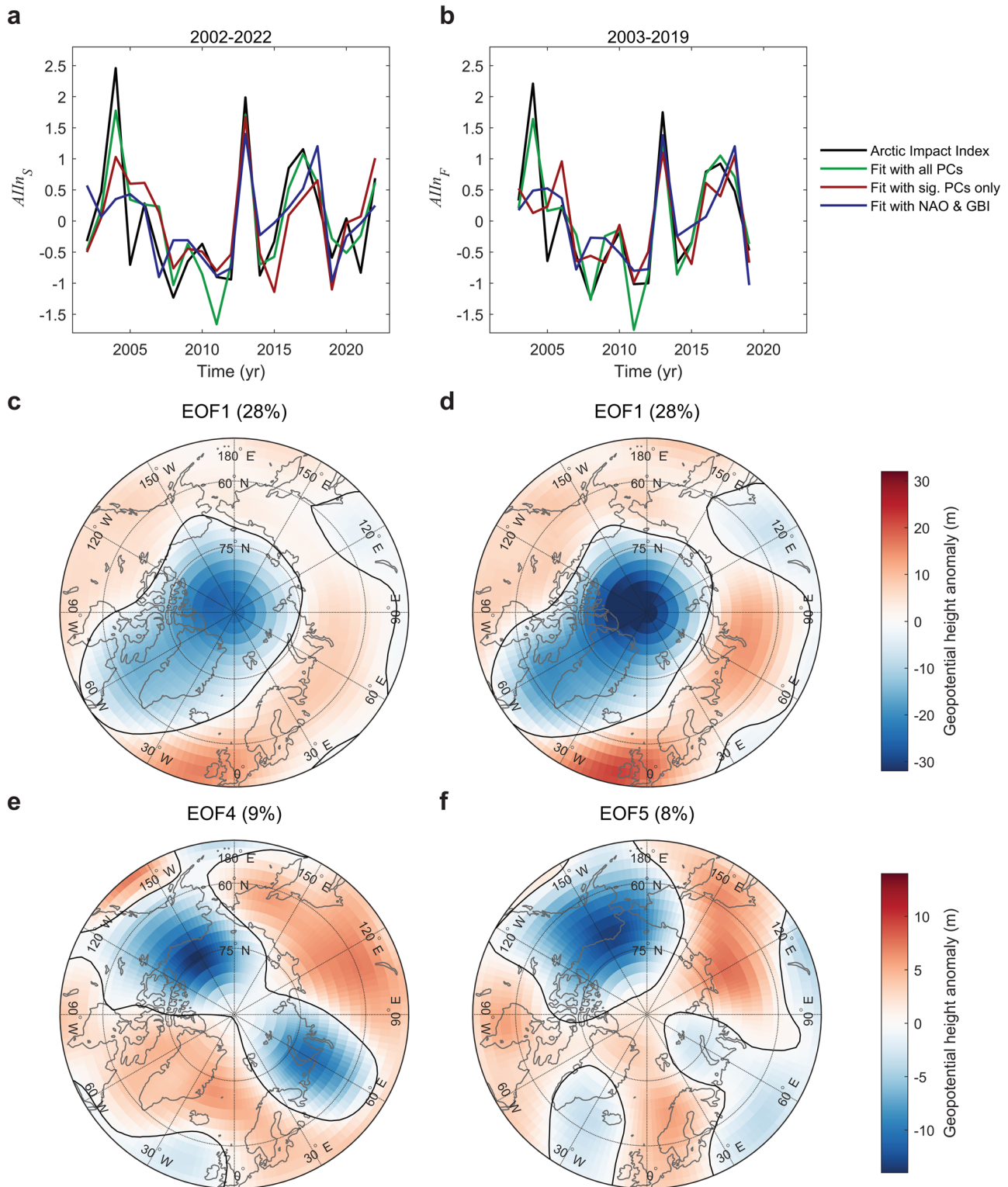
Fig. 7 | Arctic Impact Indices and primary components of atmospheric variability. Regression of **a** $AIIn_S$ (2002–2022) and **b** $AIIn_F$ (2003–2019) (both black) onto the leading principal components (green: all; red: significant) of the detrended summer mean 500 hPa geopotential height, as well as onto the summer GBI and NOA (blue). Values in brackets refer to the percentage variance explained by the respective EOF mode. **c, e** show the spatial patterns corresponding to the principal components that are significantly correlated with $AIIn_S$ (2002–2022), **d, f** are the same as **c, e** but for $AIIn_F$ (2003–2019). The spatial patterns are scaled by the regression factor of the respective principal component. The explained variance is noted in brackets.

and moisture particularly to western Greenland[60]. Therefore, similar atmospheric conditions drive the impacts in the wider Arctic, including parts of Greenland, which is the dominant source of ice-mass change in the Arctic and holds a high potential for long-term future sea-level rise[61].

We emphasize the limitation of our approach posed by isolating, per design, large-scale covariations between regions and systems. Local variations in glacier mass or active layer thickness, which do not synchronize with the larger regional patterns are filtered out in the factor analysis
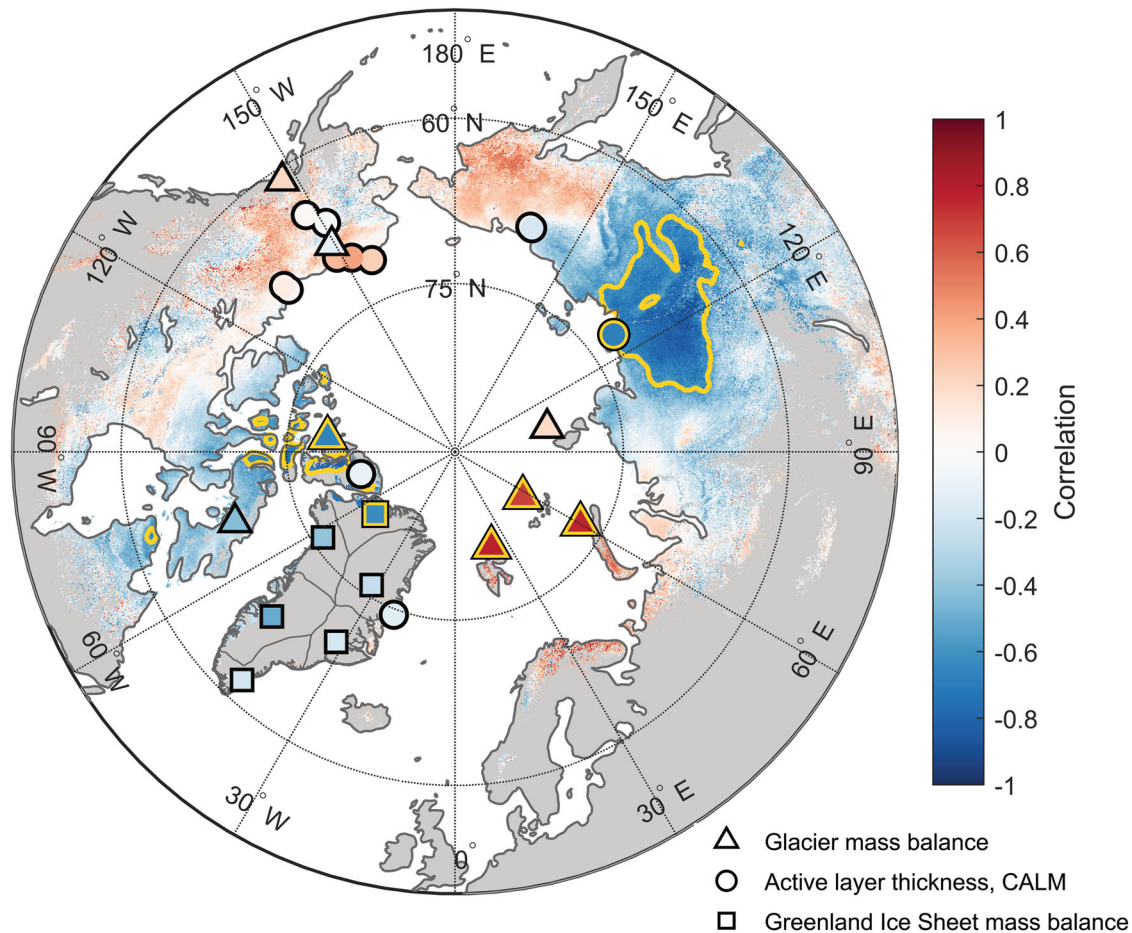
Fig. 8 | Correlation of Arctic Impact Indices with observations of changes in glacier mass and active layer thickness. Correlation (lag zero) of $AIIn_F$ with the active layer thickness from CCI (spatial pattern) and selected CALM sites (circles), as well as mass changes of the glaciers systems (triangles) and within drainage basins of the Greenland Ice Sheet (squares) for the time period 2003–2019. Significance (*p*-value < 0.05), accounting for autocorrelation in the observations and index, are indicated as yellow contours for the CCI data and yellow framed symbols for the other data.

and remain a residual signal of the time series. In turn this means that our indices based on the covariations are of limited use when representing the temporal variations at specific locations, as indicated by rather weak correlations with in situ measurements (Fig. 8). Even though we consider the pan-Arctic atmospheric conditions related the covariations a background signal at these local sites, we emphasize that understanding and interpreting the local measurements requires a regional focus in terms of the atmospheric forcing, while considering site-specific factors.

For the year 2012, our indices reflect particularly warm summer conditions for eastern parts of Northern Arctic Canada and Western Greenland (sector S2), coinciding with extreme temperatures for at least three consecutive days during summer in the longitude range 0°W to 90°W[33] (Fig. 5a). Likewise, a summer heat wave occurred in 2013 within 0°E to 90°E[33] of longitude consistent with more mass loss in Svalbard and increased active layer thickness in European Russian Arctic (sector 3b), as captured by our indices. However, at Samoylov station a record active layer thickness was measured in 2010, not reflected in our indices. Also, the Siberian heat wave in 2020 is not represented in our index based on summer means (JJA), as it already ended mid-of-June[62]. This mismatch exemplifies the limitation of our indices to represent impact signatures at specific locations, as they are constructed to isolate shared covariations between larger regions.

We have shown for the time period 2002–2022 that the atmospheric variations driving covarying impacts contain combined features NAO and GBI patterns (Figs. 6 and 7c, d), which have been shown to significantly anti-correlate and substantially control melt conditions in Greenland[32,63].

However, our study identified another relevant atmospheric circulation pattern of higher atmospheric wave number affecting the recovered covariation among Arctic systems apart from Alaska (Fig. 7e, f). This pattern is not connected to the NAO and GBI, nor the Pacific Decadal Oscillation, and reflects only 9% of atmosphere variability. But it is almost equally important as EOF1/PC1 in representing the covariations enhancing the sectorial patterns of opposite behavior. Particularly, the impacts in the year 2004 are poorly represented by the EOF1/PC1 (NAO and GBI) alone (Fig. 7a, b) and require this second mode (Fig. 7c, d).

Our analysis is limited to years after 2002 by the availability of satellite data and therefore reveals characteristics of the past two decades only. Previous studies have indicated that Arctic summer circulation patterns similar to our EOF1/PC1 are prevalent after 2000[49], particularly after 2007, with positive and high values of the GBI[32,64]. Arctic amplification and feedbacks related to shifts in circulation patterns remain a matter of debate[5,35], as some studies suggest the role of sea ice loss[65] and spring snow cover[66] in enhancement of the GBI-related conditions. In-line with blocking patterns related to EOF1 is a slower eastward propagation of atmospheric patterns with higher wave numbers[67], possibly similar to the EOF of secondary importance. Reconstructing glacier mass and active layer thickness changes using modelling approaches enabling longer time series may help to infer multi-decadal shifts in circulation patterns.

Our analysis has shown that different time series based on satellite gravimetry, remote sensing/modelling and selected in situ observations of active layer thickness record covarying impacts across the Arctic caused by the same large-scale atmospheric driving patterns (Fig. 8). Such synoptic

forcing are important to enable regional records in meltwater runoff[68] and permafrost thaw depth, or related environmental hazards like heat waves[33,62] and forest fires[55,69], but need to be understood together with long-term warming trends and system- and site specific pre-conditioning factors and local weather conditions. Therefore, climate models have to capture the dynamic changes together with thermodynamic and system-specific feedbacks to project the impact of future of glacier and permafrost systems in an increasing warmer Arctic.

Methods

Glacier mass balances from GRACE/GRACE-FO gravity fields

We derived annual mass balances from GRACE/GRACE-FO data for the following eight Arctic glacier systems: Alaska Gulf of Alaska (ALGO), Alaska North Slope Borough (ALNO), Arctic Canada North (CANN; >74°N), Arctic Canada South (CANS < 74°N), Franz Josef Land (FRJO), Novaya Zemlya (NOZE), Severnaya Zemlya (SEZE) and Svalbard (SVAL) (Fig. 1). The definition of the glacier systems follows Wouters et al.[15], and is based on the Randolph Glacier Inventory Version 6.0[42]. We utilized GRACE and GRACE-FO data from 222 mean monthly gravity field solutions spanning from April 2002 until June 2023, with a data gap of eleven months between June 2017 (last GRACE solution) and June 2018 (first GRACE-FO solution). We used release six (RL06) Level 2 gravity field solutions provided by the Science Data Systems Centres (SDS), including the Center for Space Research at the University of Texas (CSR; RL6.2), Jet Propulsion Laboratory (JPL; RL6.1), and GFZ German Research Centre for Geosciences (GFZ; RL6.1). We followed the method originally proposed by in ref. 70 and adapted in ref. 49 to combine these solutions for coefficients up to degree and order 60, reducing noise and outlier effects.

Following the recommendation of the SDS centers, we inserted degree-1 coefficients not provided by GRACE/GRACE-FO with estimates of[71] available as GRACE Technical Note 13[72], and replaced the uncertain C_{20}, as well as C_{30} coefficients starting August 2016, in the GRACE/GRACE-FO by satellite-laser ranging estimates provided in GRACE Technical Note 14[73,74], respectively.

To correct for glacial isostatic adjustment (GIA) linear trends in the gravity field, we applied the ICE6G Model[75]. We subtracted the linear trend resulting from hydrological variations, as well as GIA related to changes since the Little Ice Age, based on the average of the two models presented in ref. 15. However, we did not consider any non-linear effects of both corrections. Uncertainties in the GIA corrections are taken from[15] and added to the propagated uncertainties of the GRACE/GRACE-FO linear trends. Note that GIA is considered to occur at constant rates and is therefore removed by subsequent detrending of the data in further analysis.

Signal leakage out of the domain of interest caused by the limited spectrum of GRACE/GRACE-FO coefficients (here, up to degree and order 60) is mitigated by the use of adjusted forward models, for which signals are extrapolated up to degree and order 256. Noise leakage into the domain of interest is small for glacier systems surrounded by ocean, as gravity signals from proximal ocean mass variability are removed by the SDS centres during production of GRACE/GRACE-FO Level-2 data. In addition, a geographical mask including all RGI6.0 regions was applied to the GRACE/GRACE-FO data in spectral domain[76] to reduce leakage of mass signals from non-glaciated areas.

We estimated changes in ice mass using GRACE/GRACE-FO gravity field observations at time t_i. We employed a forward-modelling based inversion approach in the spatial domain, as detailed described in ref. 49, which is an adaptation of the approach previously applied to Greenland[60,77] and Antarctica[78]. We derived annual mass balances by fitting a piecewise linear regression model with annual segments, each of which starting 1 January of each year to the monthly GRACE/GRACE-FO time series. After that, we detrended the annual mass balances and annual active layer thickness with a first-order polynomial fit (order $n = 1$) to isolate interannual mass variations. Finally, to facilitate direct comparisons of measurements across regions and observation types, we standardized the detrended time series by scaling it to have a mean of zero and a standard deviation of one.

It is important to note that the annual balances for 2002 are based on only seven observations, those for 2017 and 2018 only on five monthly gravity solutions, increasing the uncertainty of the annual balances for these years by a factor of 1.4. As the factor analysis relies on continuous (yearly) data, we accept this shortcoming instead of mitigating it by estimation of bi-annual averages as in ref. 60. We then removed the mean and linear trend of the annual balances for 2002–2022 to determine the interannual balance variations. This step was taken to eliminate any possible long-term changes of the annual mass balances associated with an acceleration or deceleration of mass change.

To quantify uncertainties, we propagated the monthly data uncertainty to the annual balances. Furthermore, we compared our annual mass balance estimates for the period of 2003–2019 with time series derived by ref. 15 using a different gravimetric inversion approach (update to November 2019 by the authors; 179 monthly solutions). The uncertainties (1σ) for the annual mass balance anomalies consist of propagated uncertainties of the GRACE/GRACE-FO solutions and the inversion method differences, and are ± 41 Gt yr^{-1} (ALGO), ± 10 Gt yr^{-1} (ALNO), ± 11 Gt yr^{-1} (CANN), ± 12 Gt yr^{-1} (CANS), ± 7 Gt yr^{-1} (FRJO), ± 8 Gt yr^{-1} (NOZE), ± 7 Gt yr^{-1} (SEZE) and ± 8 Gt yr^{-1} (SVAL).

Active layer thickness

CALM in situ measurements. We estimated the active layer thickness using in-situ measurements provided by the CALM network[43]. Established in 1991, CALM consists of more than 200 measurement sites in 15 countries measuring active layer thickness[39,43] https://www2.gwu.edu/~calm/. The active layer thickness is derived from the end-of-season thaw depth obtained using mechanical probing, thaw tubes, or thermistors placed in the ground or boreholes to log depth-dependent temperature profiles[46,47]. Recent regional results of trends from CALM in situ observations in the Arctic are summarized elsewhere[11].

The CALM dataset includes annual end-of-season thaw depth for 1990–2023, although there are sometimes temporal data gaps (https://www2.gwu.edu/~calm/). For our analysis, we limit our focus to stations located north of latitude 60°N to specifically examine changes of the active layer thickness in Arctic permafrost.

We expand the CALM network dataset by incorporating data from the Bayelva station near Ny-Ålesund, Svalbard, which provides long-term measurements of multiple climate and subsurface parameters from a long term permafrost observatory, located on West Spitsbergen[79]. For our analysis, we use thermistor measurements of soil/permafrost temperature at depths up to 1.3 m for the time period 1998–2017 (Level 2 data available at https://doi.org/10.1594/PANGAEA.948951). As the thermistors record maximum temperatures above zero for all depths down to 1.3 m since 2004, we cannot infer the active layer thickness. Instead, as proxy, we determine the changes in the zero crossing of the depth-temperature profile obtained from the thermistor measurements at a fixed point in time - here, the midpoint of July of each year for the site of Bayelva. We omitted the year 2014, for which we could not infer a zero crossing of the depth-temperature profile as all thermistors showed below zero temperatures in mid-of-July.

The CALM data set includes active layer thickness estimates from the long-term observational site Samoylov, located in the Lena River Delta of northern Siberia (72.37°N, 126.48°E). The research site is situated in a region with cold and arid tundra climate conditions, providing a wide range of meteorological, surface and sub-surface parameters. The active layer thickness is measured by mechanical probing, usually between June and July and the end of August since the year 2002[45]. Similar to other CALM sites, probing in summer does not necessarily capture the maximum thaw depth.

CCI remote sensing and modelling data. We utilize active layer product of the CCI_Permafrost project of ESA to obtain estimates of regional and sectorial averages of the active layer thickness in the Arctic for the period 2003–2019 (https://climate.esa.int/en/projects/permafrost/). This project provides information on permafrost ground temperature, active layer depth, and permafrost extent globally, by combining estimates of

land surface temperature data from NASA satellites Terra and Aqua, re-analysis data on snow water equivalent, and landcover/vegetation types. The CryoGrid CCI thermal model, which integrates these data sources, was used to estimate the thermal regime of the ground[44,80,81]. The resulting data product, Permafrost_CCI version 3, provides active layer thickness and permafrost extent fractions at a spatial resolution of 1 km[25]. To focus on regional variability, we reduced the spatial resolution to 10 km using nearest neighbour interpolation.

Selecting CALM locations. We selected a subset of the 266 field measurements (CALM network and Bayelva station) that offer the best nearly continuous representation of regional Arctic permafrost change. Firstly, we only considered stations located north of 60°N, resulting in 185 records, among which 120 represent continuous permafrost (in our study, however, all permafrost types allowed). For 185 CALM stations north of 60°N interannual variations range between several centimetres to decimetres (10–49 cm for 10–90% percentile)[39,43].

Next, we selected only nearly continuous time series for the years 2003–2017 by filtering out records with more than one missing annual value (57 records remaining) and removed one record from the Abisko area, Northern Sweden (56 records remaining).

Finally, we observed that four co-located sites at Mt. Rodinka, Russia (R18, R18a, R30A, and R30B) exhibited high correlation with each other ($r > 0.9$), and to avoid an oversampling bias, we selected a single 10 m grid measurement represented by station code R18a, which offers the most up-to-date measurements, resulting in a final selection of 53 in situ records of permafrost change.

Next, we evaluated the CALM records in terms of their representativeness for regional changes (Supplementary Fig. 1). This step was necessary as CALM in situ time series may be dominated by site-specific, local variability, as well as measurement noise and artefacts. Omission of these data possibly neglects information on permafrost change and related process, but at the same time ensures that the variability is not dominated by local impacts. We therefore end up limiting our analysis to 15 records that show significant correlation with the nearest grid point of the CCI remote sensing product, accounting for auto-correlation by reducing the number of degrees of freedom when determining the critical threshold for significance, following the approach of[82]. As the CALM time series are discontinuous, we adopted the auto-correlation determined for the continuous Permafrost_CCI data at the specific CALM sites.

To address double sampling owing to using different techniques at co-located sites, we applied hierarchical clustering based on geographical distance, grouping all sites within a range of 1000 m and calculating the unweighted averages of their anomalies as a representation of the cluster. We also inserted Permafrost_CCI data for nine of 13 selected CALM time series to obtain continuous records for 2003–2019.

Finally, for some stations, different measurements techniques were used at nearby locations. At the 13 selected sites, the most commonly used measurement technique was mechanical probing (U1 & U2, U8, U16, R51, R17, R18A, R21, and U19) and thaw tubes (C5A and C7A). Although C18 does have thaw tubes the value reported is based on mechanical probing on a grid. On site U22, borehole temperatures were used to infer active layer thickness. Eleven of the 13 sites were located on continuous permafrost, and two on discontinuous permafrost. To estimate uncertainties, we calculated the standard deviation of the difference between the CALM and CCI data at the selected sites. We assumed that these deviations are equally caused by noise in the CALM and CCI data, and therefore equally attribute uncertainties to both time series of annual active layer thickness anomalies. For the CCI regional and sectorial averages, we adopted the median uncertainty attributed to the CCI data at the CALM locations. Comparisons of absolute values of active layer thickness of the selected CALM and CCI Permafrost data sets has been part of the EO4PAC project[83].

The 13 CALM sites selected are: AVBA, Barrow, Alaska North Slope (71.34°N, −156.59°E), Site code: U1 & U2 (averaged); FRAN, Franklin Bluff,

Alaska North Slope (69.7°N, −148.72°E), Site code: U8; FISH, Fish Creek, Alaska North Slope (70.36°N, −152.05°E), Site code: U22; OLDM, Old Man, Alaska Interior (66.48°N, −150.62°E), Site code: U16; PEAR, Pearl Creek, Alaska Interior (64.94°N, −147.82°E), Site code: U19; LOUS, Lousy Point (Thaw tube), North Canada (69.25°N, −134.29°E), Site code: C5A; REIN, Reindeer Depot (Thaw tube), North Canada (68.72°N, −134.15°E), Site code: C7A; TANQ, Tanquary Fiord, Ellesmere Island, North Canada (81.41°N, −76.71°E), Site code: C18; SAMO, Samoylov, Central Siberia (72.37°N, 126.48°E), Site code: R51; AKHM, Akhmelo channel, Kolyma, North East Siberia (68.85°N, 161°E), Site code: R17; MTRO, Mt. Rodinka, Kolyma (10 m grid), North East Siberia (68.77°N, 161.5°E), Site code: R18A; LAKE, Lake Akhmelo, Kolyma, North East Siberia (68.86°N, 161.03°E), Site code: R21; AVZA, Zackenberg, Greenland (74.49°N, −20.56°E), Site codes: G1 & G2 (averaged). This information is also tabulated in the Supplementary Table.

Atmosphere re-analyses and indices
In this study, we utilized atmospheric re-analysis data provided by the NCEP[52]. The NCEP data consists of monthly means of geopotential height at 500 hPa (z500) and air temperature at geopotential height 700 hPa (t700), with a spatial resolution of 2.5° × 2.5°, covering the time period from 1979 to present (https://psl.noaa.gov/data/gridded/data.ncep.reanalysis2.html).

Factor analysis
We applied factor analysis[84,85] to identify shared variation in the time series of glacier mass balance and permafrost active layer thickness. The goal of factor analysis is to elucidate covariant relationships among observed variables with a few underlying unobserved factors (typically one to three). Highly correlated variables are grouped together so that their correlation with other groups is minimized. These groups are known as factors and reflect the correlation structure[84].

To describe the relationship between factors and variables, we followed[48] and expressed it as

$$\mathbf{x} = \boldsymbol{\mu} + \boldsymbol{\Lambda}\mathbf{f} + \mathbf{e}$$

where each element of $\mathbf{x}$ is a vector of observations, $\boldsymbol{\mu}$ is the mean of each of these vectors, $\mathbf{f}$ is the common factor vector and $\boldsymbol{\Lambda}$ is the factor loading matrix that connects the factors with certain weights to the observables. The variable $\mathbf{e}$ is the independent or specific factor vector, sometimes called error vector, as it is unique for every variable and cannot be explained by the common factors[84]. The factor loading matrix $\boldsymbol{\Lambda}$ describes the strength of the relationship between variables and factors[85]. The variance explained by the common factors is called communality and is represented by the square of the factor loadings. The variance that is not explained by the common factors is the specific or unique variance[85].

Arctic Impact Index
We conducted a factor analysis to identify the primary mode of covariation between Arctic glacier mass balance and permafrost changes. Our analysis focused on the years 2003–2019, which allowed for maximum overlap between GRACE/GRACE-FO and CCI data. However, based on the results of the factor analysis, we extended the generation of the Arctic Impact Index to 2002–2022, including only GRACE/GRACE-FO and CALM data for 2002, 2020–2022. As we only had 17 annual balances for each location, we limited the factor analysis to ten locations at a time and two common factors. To ensure that all locations were considered, we randomized the selection process and repeated the factor analysis for an ensemble of more than 135,884 members, with the condition that at least one observation was located in each of the five sectors shown in Fig. 1.

The ensemble members were constrained using post-analysis criteria modified from[48]: i) a threshold of >0.3 has to be exceeded for overall consideration of the factor loading of an observation $|\Lambda|$; ii) factor loading $|\Lambda| \geq 0.6$ is considered significant, and, iii) if loading of factor 1 is significant $|\Lambda| \geq 0.6$, loading of factor 2 has to be below <0.3 in order to consider the

observation. In total, we selected 98 members showing at least three significant positive and three significant negative factor loadings on the first factor. Additionally, we included an ensemble member dominated by GRACE/GRACE-FO observations (eight glacier systems), supplemented by permafrost change in central parts of Siberia (PEVE) and the Lena delta (LENA), even if the factor loadings did not fulfil the criteria above.

After constraining the ensemble, we pursued two methods to compute the Arctic Impact Index. The first approach uses the scores of the first factor obtained directly from the factor analyses, and we applied standardization, $AIIn_F(t_i) = f_1(t_i)/std(f_1)$. Alternatively, we selected regions with significant loading factors to enter the computation of the Arctic Impact Index according to $Z(t_i) = \sum_{n=1}^{N} \alpha_n z_n(t_i)$, where $\alpha = -1$, if $\Lambda_{1,n} < 0$ and $\alpha = +1$, if $\Lambda_{1,n} > 0$, and $z(t_i)$ are standardized anomalies of the time series of each observation. The time variation of the index was obtained with double standardization $AIIn_S(t_i) = Z(t_i)/std(Z)$. The time series-based index enabled us to extend the time period to 2002--2022, despite gaps and periods of solely GRACE/GRACE-FO and CALM observations.

We calculated the means and standard deviations of the 98 ensemble members for $AIIn_F(t_i)$ and $AIIn_S(t_i)$. To reflect uncertainties of the input data in the index $AIIn_S(t_i)$, we propagated the uncertainty associated with the time series entering each member to the index and added this to the ensemble standard deviation.

Correlation of atmospheric variables and Arctic Impact Index
We evaluated the relationship between the summer (JJA) mean of the atmospheric variables z500 and t700 (Fig. 4) with both the Arctic Impact Indices, the $AIIn_F$ (2003–2019) and $AIIn_S$ (2002–2022), using the Pearson correlation coefficient of lag zero. To assess the statistical significance of the correlation, we applied a critical value of 5% (p-value < 0.05) using surrogate time series based on phase scrambling[86] to account for autocorrelation in the time series of the indices and the atmosphere variable at each grid point.

Empirical orthogonal functions analysis
To isolate the variability of large-scale atmospheric circulation patterns in the set of atmospheric variables, we employed Empirical Orthogonal Functions (EOFs)[87]. The atmospheric fields were weighted spatially using $\sqrt{\cos(\vartheta)}$, which varies depending on latitude, ϑ. We calculated the EOFs using the Climate Data Toolbox for Matlab[88].

Data availability
The CALM data can be accessed at https://www2.gwu.edu/~calm/data/north.htm. Time series of soil temperature measurements at Bayelva, Svalbard, are available at https://doi.org/10.1594/PANGAEA.948951[79]. For Samoylov station, Siberia, actively layer thickness, as well as multiple climate and subsurface parameters can be downloaded at https://doi.org/10.1594/PANGAEA.947032[45]. The ESA Climate Change Initiative Permafrost data and relevant documentation are available from https://climate.esa.int/en/projects/permafrost/data/ and https://climate.esa.int/de/projekte/permafrost/key-documents/, respectively[89]. GRACE/GRACE-FO gravity fields (Level 2 data) and supporting documentation can be freely accessed from the websites of the Science Data Systems Centres, available at http://podaac.jpl.nasa.gov and http://isdc.gfz-potsdam.de, respectively. The North Atlantic Oscillation (NAO) Index can be downloaded from https://www.ncei.noaa.gov/access/monitoring/nao/. The Greenland Blocking Index (GBI) is available from https://psl.noaa.gov/gcos_wgsp/Timeseries/Data/gbi.mon.data. NCEP Reanalysis data are available from the following source: https://psl.noaa.gov/data/gridded/data.ncep.reanalysis2.html (NCEP/DOE Reanalysis II). Source data for the reproduction of Figs. 1 through 8 are available for download[90].

Code availability
Spherical harmonic functions were managed using the software package developed by Frederik J. Simons, which is available at http://geoweb.princeton.edu/people/simons/software.html (last accessed on 5 June 2024).

Empirical Orthogonal Functions (EOFs) were calculated using the Climate Data Toolbox for MATLAB[88]. Factor analysis, along with other statistical analyses and visualization of the results, were conducted using MATLAB (version R2022b, MathWorks Inc., Natick, MA, USA).

References
1. Intergovernmental Panel On Climate Change (IPCC). *The Ocean and Cryosphere in a Changing Climate: Special Report of the Intergovernmental Panel on Climate Change*. (Cambridge University Press, 2022). https://doi.org/10.1017/9781009157964.
2. Rantanen, M. et al. The Arctic has warmed nearly four times faster than the globe since 1979. *Commun. Earth Environ.* **3**, 168 (2022).
3. Cohen, J. et al. Recent Arctic amplification and extreme mid-latitude weather. *Nat. Geosci.* **7**, 627–637 (2014).
4. Francis, J. A. & Vavrus, S. J. Evidence for a wavier jet stream in response to rapid Arctic warming. *Environ. Res. Lett.* **10**, 014005 (2015).
5. Screen, J. A., Bracegirdle, T. J. & Simmonds, I. Polar Climate Change as Manifest in Atmospheric Circulation. *Curr. Clim. Change Rep.* **4**, 383–395 (2018).
6. Box, J. E. et al. Key indicators of Arctic climate change: 1971–2017. *Environ. Res. Lett.* **14**, 045010 (2019).
7. Moon, T. A. NOAA Arctic Report Card 2021 Executive Summary. https://doi.org/10.25923/5S0F-5163 (2021).
8. Myers-Smith, I. H. et al. Complexity revealed in the greening of the Arctic. *Nat. Clim. Change* **10**, 106–117 (2020).
9. Hugonnet, R. et al. Accelerated global glacier mass loss in the early twenty-first century. *Nature* **592**, 726–731 (2021).
10. Biskaborn, B. K. et al. Permafrost is warming at a global scale. *Nat. Commun.* **10**, 264 (2019).
11. Smith, S. L. et al. Permafrost. In *State of the Climate in 2022* vol. 4 301–305 (Bull. Amer. Meteor. Soc., 2023).
12. Intergovernmental Panel On Climate Change. *Climate Change 2021 – The Physical Science Basis: Working Group I Contribution to the Sixth Assessment Report of the Intergovernmental Panel on Climate Change*. (Cambridge University Press, 2023). https://doi.org/10.1017/9781009157896.
13. Mudryk, L. et al. Historical Northern Hemisphere snow cover trends and projected changes in the CMIP6 multi-model ensemble. *The Cryosphere* **14**, 2495–2514 (2020).
14. Meier, W. N. et al. Sea ice. In *State of the Climate in 2022* vol. 9 290–293 (Bull. Amer. Meteor. Soc., 2023).
15. Wouters, B., Gardner, A. S. & Moholdt, G. Global glacier mass loss during the GRACE satellite mission (2002-2016). *Front. Earth Sci.* **7**, 96 (2019).
16. Shepherd, A. et al. Mass balance of the Greenland Ice Sheet from 1992 to 2018. *Nature* **579**, 233–239 (2020).
17. Handorf, D., Jaiser, R., Dethloff, K., Rinke, A. & Cohen, J. Impacts of Arctic sea ice and continental snow cover changes on atmospheric winter teleconnections. *Geophys. Res. Lett.* **42**, 2367–2377 (2015).
18. Miner, K. R. et al. Permafrost carbon emissions in a changing Arctic. *Nat. Rev. Earth Environ.* **3**, 55–67 (2022).
19. Marzeion, B. et al. Partitioning the Uncertainty of Ensemble Projections of Global Glacier Mass Change. *Earths Future* **8**, (2020).
20. Smith, S. L., O'Neill, H. B., Isaksen, K., Noetzli, J. & Romanovsky, V. E. The changing thermal state of permafrost. *Nat. Rev. Earth Environ.* **3**, 10–23 (2022).
21. Schuur, E. A. G. et al. Permafrost and Climate Change: Carbon Cycle Feedbacks From the Warming Arctic. *Annu. Rev. Environ. Resour.* **47**, 343–371 (2022).
22. Schuur, E. A. G. et al. Climate change and the permafrost carbon feedback. *Nature* **520**, 171–179 (2015).

23. Box, J. E. et al. Global sea-level contribution from Arctic land ice: 1971–2017. *Environ. Res. Lett.* **13**, 125012 (2018).

24. Van Everdingen, R. O. & International Permafrost Association Terminology Working Group. *Multi-Language Glossary of Permafrost and Related Ground-Ice Terms in Chinese, English, French, German, Icelandic, Italian, Norwegian, Polish, Romanian, Russian, Spanish, and Swedish*. (International Permafrost Association, Terminology Working Group, 1998).

25. Westermann, S., Bartsch, A. & Strozzi, T. CCI+ Permafrost D2.2 Algorithm Theoretical Basis Document (ATBD). (2020).

26. Van Everdingen, R. O., Association, I. P., & others. *Multi-Language Glossary of Permafrost and Related Ground-Ice Terms in Chinese, English, French, German…* (Arctic Inst. of North America University of Calgary, 1998).

27. O'Neill, H. B., Smith, S. L., Burn, C. R., Duchesne, C. & Zhang, Y. Widespread Permafrost Degradation and Thaw Subsidence in Northwest Canada. *J. Geophys. Res. Earth Surf.* **128**, e2023JF007262 (2023).

28. Vasiliev, A. A. et al. Permafrost degradation in the Western Russian Arctic. *Environ. Res. Lett.* **15**, 045001 (2020).

29. Nyland, K. E. et al. Long-term Circumpolar Active Layer Monitoring (CALM) program observations in Northern Alaskan tundra. *Polar Geogr* **44**, 167–185 (2021).

30. Burke, E. J., Zhang, Y. & Krinner, G. Evaluating permafrost physics in the Coupled Model Intercomparison Project 6 (CMIP6) models and their sensitivity to climate change. *The Cryosphere* **14**, 3155–3174 (2020).

31. Rajewicz, J. & Marshall, S. J. Variability and trends in anticyclonic circulation over the Greenland ice sheet, 1948–2013. *Geophys. Res. Lett.* **41**, 2842–2850 (2014).

32. Silva, T. et al. The impact of climate oscillations on the surface energy budget over the Greenland Ice Sheet in a changing climate. *The Cryosphere* **16**, 3375–3391 (2022).

33. Dobricic, S., Russo, S., Pozzoli, L., Wilson, J. & Vignati, E. Increasing occurrence of heat waves in the terrestrial Arctic. *Environ. Res. Lett.* **15**, 024022 (2020).

34. Neff, W., Compo, G. P., Martin Ralph, F. & Shupe, M. D. Continental heat anomalies and the extreme melting of the Greenland ice surface in 2012 and 1889: Melting of Greenland in 1889 and 2012. *J. Geophys. Res. Atmo.* **119**, 6520–6536 (2014).

35. Shepherd, T. G. Atmospheric circulation as a source of uncertainty in climate change projections. *Nat. Geosci.* **7**, 703–708 (2014).

36. Hanna, E., Cropper, T. E., Hall, R. J. & Cappelen, J. Greenland Blocking Index 1851-2015: a regional climate change signal. *Int. J. Climatol.* **36**, 4847–4861 (2016).

37. Delhasse, A., Hanna, E., Kittel, C. & Fettweis, X. Brief communication: CMIP6 does not suggest any circulation change over Greenland in summer by 2100. *Cryosphere Discuss* **2020**, 1–8 (2020).

38. Carvalho, K. S. & Wang, S. Sea surface temperature variability in the Arctic Ocean and its marginal seas in a changing climate: Patterns and mechanisms. *Glob. Planet. Change* **193**, 103265 (2020).

39. Nelson, F. E., Shiklomanov, N. I. & Nyland, K. E. Cool, CALM, collected: the Circumpolar Active Layer Monitoring program and network. *Polar Geogr.* **44**, 155–166 (2021).

40. Flechtner, F., Morton, P., Watkins, M. & Webb, F. Status of the GRACE Follow-On Mission. In *Gravity, Geoid and Height Systems* (ed. Marti, U.) Vol. 141 117–121 (Springer International Publishing, Cham, 2014).

41. Tapley, B. D. et al. Contributions of GRACE to understanding climate change. *Nat. Clim. Change* **9**, 358–369 (2019).

42. RGI Consortium, Randolph Glacier Inventory - A Dataset of Global Glacier Outlines, Version 6. https://doi.org/10.7265/4m1f-gd79 (2017).

43. Hinkel, K. M. Spatial and temporal patterns of active layer thickness at Circumpolar Active Layer Monitoring (CALM) sites in northern Alaska, 1995–2000. *J. Geophys. Res.* **108**, 8168 (2003).

44. Westermann, S. et al. The CryoGrid community model (version 1.0) – a multi-physics toolbox for climate-driven simulations in the terrestrial cryosphere. *Geosci. Model Dev. Discuss.* **2022**, 1–61 (2022).

45. Boike, J. et al. A 16-year record (2002–2017) of permafrost, active-layer, and meteorological conditions at the Samoylov Island Arctic permafrost research site, Lena River delta, northern Siberia: an opportunity to validate remote-sensing data and land surface, snow, and permafrost models. *Earth Syst. Sci. Data* **11**, 261–299 (2019).

46. Brown, J., Hinkel, K. M. & Nelson, F. E. The circumpolar active layer monitoring (calm) program: Research designs and initial results. *Polar Geogr* **24**, 166–258 (2000).

47. Humlum, O. & Matsuoka, N. A handbook on periglacial field methods. *Int. Permafr. Assoc. Work. Group Periglac. Proc Environ.*, **82**, last accessed 12 July 2024, https://www2.gwu.edu/~calm/research/A_Handbook_on_Periglacial_Field_Methods_20040406.pdf (2004).

48. Overland, J. E., Wang, M. & Box, J. E. An integrated index of recent pan-Arctic climate change. *Environ. Res. Lett.* **14**, 035006 (2019).

49. Sasgen, I. et al. Arctic glaciers record wavier circumpolar winds. *Nat. Clim. Change* **12**, 249–255 (2022).

50. Zhang, T. & Stamnes, K. Impact of climatic factors on the active layer and permafrost at Barrow, Alaska. *Permafr. Periglac. Process.* **9**, 229–246 (1998).

51. Strand, S. M., Christiansen, H. H., Johansson, M., Åkerman, J. & Humlum, O. Active layer thickening and controls on interannual variability in the Nordic Arctic compared to the circum-Arctic. *Permafr. Periglac. Process.* **32**, 47–58 (2021).

52. Kalnay, E. et al. The NCEP/NCAR 40-Year Reanalysis Project. *Bull. Am. Meteorol. Soc.* **77**, 437–472 (1996).

53. Van Pelt, W. & Kohler, J. Modelling the long-term mass balance and firn evolution of glaciers around Kongsfjorden. *Svalbard. J. Glaciol.* **61**, 731–744 (2015).

54. Van Pelt, W. J. J., Pohjola, V. A. & Reijmer, C. H. The changing impact of snow conditions and refreezing on the mass balance of an idealized svalbard glacier. *Front. Earth Sci.* **4**, 102 (2016).

55. Kim, J.-S., Kug, J.-S., Jeong, S.-J., Park, H. & Schaepman-Strub, G. Extensive fires in southeastern Siberian permafrost linked to preceding Arctic Oscillation. *Sci. Adv.* **6**, eaax3308 (2020).

56. Jan, A. & Painter, S. L. Permafrost thermal conditions are sensitive to shifts in snow timing. *Environ. Res. Lett.* **15**, 084026 (2020).

57. Pascual, D. & Johansson, M. Increasing impacts of extreme winter warming events on permafrost. *Weather Clim. Extrem.* **36**, 100450 (2022).

58. McLeod, J. T., Ballinger, T. J. & Mote, T. L. Assessing the climatic and environmental impacts of mid-tropospheric anticyclones over Alaska. *Int. J. Climatol.* **38**, 351–364 (2018).

59. Atkinson, D. E. et al. Canadian cryospheric response to an anomalous warm summer: A synthesis of the Climate Change Action Fund Project "The State of the Arctic Cryosphere during the Extreme Warm Summer of 1998. *Atmosphere-Ocean* **44**, 347–375 (2006).

60. Sasgen, I. et al. Return to rapid ice loss in Greenland and record loss in 2019 detected by the GRACE-FO satellites. *Commun. Earth Environ.* **1**, 8 (2020).

61. Hanna, E. et al. Short- and long-term variability of the Antarctic and Greenland ice sheets. *Nat. Rev. Earth Environ.* **5**, 193–210 (2024).

62. Overland, J. E. & Wang, M. The 2020 Siberian heat wave. *Int. J. Climatol.* **41**, E2341–E2346 (2021).

63. Tedesco, M. et al. Arctic cut-off high drives the poleward shift of a new Greenland melting record. *Nat. Commun.* **7**, 11723 (2016).

64. Hanna, E., Cropper, T. E., Hall, R. J., Cornes, R. C. & Barriendos, M. Extended North Atlantic Oscillation and Greenland Blocking Indices 1800–2020 from New Meteorological Reanalysis. *Atmosphere* **13**, 436 (2022).

65. Sellevold, R., Lenaerts, J. T. M. & Vizcaino, M. Influence of Arctic sea-ice loss on the Greenland ice sheet climate. *Clim. Dyn.* **58**, 179–193 (2022).

66. Preece, J. R. et al. Summer atmospheric circulation over Greenland in response to Arctic amplification and diminished spring snow cover. *Nat. Commun.* **14**, 3759 (2023).

67. Coumou, D., Petoukhov, V., Rahmstorf, S., Petri, S. & Schellnhuber, H. J. Quasi-resonant circulation regimes and hemispheric synchronization of extreme weather in boreal summer. *Proc. Natl. Acad. Sci.* **111**, 12331–12336 (2014).

68. Noël, B. et al. Low elevation of Svalbard glaciers drives high mass loss variability. *Nat. Commun.* **11**, 4597 (2020).

69. Balzter, H. et al. Impact of the Arctic Oscillation pattern on interannual forest fire variability in Central Siberia. *Geophys. Res. Lett*. **32**, (2005).

70. Jean, Y., Meyer, U. & Jäggi, A. Combination of GRACE monthly gravity field solutions from different processing strategies. *J. Geod.* **92**, 1313–1328 (2018).

71. Sun, Y., Riva, R. & Ditmar, P. Optimizing estimates of annual variations and trends in geocenter motion and J_2 from a combination of GRACE data and geophysical models. *J. Geophys. Res. Solid Earth* **121**, 8352–8370 (2016).

72. Landerer, F. *Monthly Estimates of Degree-1 (Geocenter) Gravity Coefficients*, *Generated from GRACE (04-2002–06/2017) and GRACE-FO (06/2018 Onward) RL06 Solutions GRACE Technical Note 13*. https://podaac-tools.jpl.nasa.gov/drive/files/allData/grace/docs/TN-13_GEOC_CSR_RL06.txt (2019).

73. Loomis, B. D., Rachlin, K. E. & Luthcke, S. B. Improved Earth oblateness rate reveals increased ice sheet losses and mass-driven sea level rise. *Geophys. Res. Lett.* **46**, 6910–6917 (2019).

74. Loomis, B. D. & Rachlin, K. E. *NASA GSFC SLR C20 and C30 Solutions GRACE Technical Note 14*. https://podaac-tools.jpl.nasa.gov/drive/files/allData/gracefo/docs/TN-14_C30_C20_GSFC_SLR.txt (2022).

75. Peltier, W. R., Argus, D. F. & Drummond, R. Space geodesy constrains ice age terminal deglaciation: The global ICE-6G_C (VM5a) model. *J. Geophys. Res. Solid Earth* **120**, 450–487 (2015).

76. Martinec, Z. Program to calculate the spectral harmonic expansion coefficients of the two scalar fields product. *Comput. Phys. Commun.* **54**, 177–182 (1989).

77. Sasgen, I. et al. Timing and origin of recent regional ice-mass loss in Greenland. *Earth Planet. Sci. Lett.* **333**, 293–303 (2012).

78. Sasgen, I. et al. Antarctic ice-mass balance 2003 to 2012: regional reanalysis of GRACE satellite gravimetry measurements with improved estimate of glacial-isostatic adjustment based on GPS uplift rates. *The Cryosphere* **7**, 1499–1512 (2013).

79. Boike, J. et al. A 20-year record (1998–2017) of permafrost, active layer and meteorological conditions at a high Arctic permafrost research site (Bayelva, Spitsbergen). *Earth Syst. Sci. Data* **10**, 355–390 (2018).

80. Westermann, S. et al. Transient modeling of the ground thermal conditions using satellite data in the Lena River delta, Siberia. *The Cryosphere* **11**, 1441–1463 (2017).

81. Westermann, S. et al. Simulating the thermal regime and thaw processes of ice-rich permafrost ground with the land-surface model CryoGrid 3. *Geosci. Model Dev.* **9**, 523–546 (2016).

82. Barker, L. J., Hannaford, J., Chiverton, A. & Svensson, C. From meteorological to hydrological drought using standardised indicators. *Hydrol. Earth Syst. Sci.* **20**, 2483–2505 (2016).

83. Bartsch, A. et al. *Earth Observation for Permafrost Dominated Arctic Coasts: D2 – Product Validation Report for Shoreline Vectors & Erosion Rates, Infrastructure, and Permafrost Products*. (2023).

84. Johnson, R. A. & Wichern, D. W. *Applied Multivariate Statistical Analysis*. (Prentice Hall Upper Saddle River, NJ, 2002).

85. Yong, A. G. & Pearce, S. A beginner's guide to factor analysis: Focusing on exploratory factor analysis. *Tutor. Quant. Methods Psychol.* **9**, 79–94 (2013).

86. Theiler, J., Eubank, S., Longtin, A., Galdrikian, B. & Doyne Farmer, J. Testing for nonlinearity in time series: the method of surrogate data. *Phys. Nonlinear Phenom.* **58**, 77–94 (1992).

87. Bjerknes, J. Atmospheric teleconnections from the equatorial Pacific. *Mon. Weather Rev.* **97**, 163–172 (1969).

88. Greene, C. A. et al. The Climate Data Toolbox for MATLAB. *Geochem. Geophys. Geosystems* **20**, 3774–3781 (2019).

89. Obu, J. et al. ESA Permafrost Climate Change Initiative (Permafrost_cci): Permafrost version 3 data products. Centre for Environmental Data Analysis, last accessed 12 July 2024, https://catalogue.ceda.ac.uk/uuid/8239d5f6263f4551bf2bd100d3ecbead (2024).

90. Sasgen, I. "Replication Data for: Atmosphere circulation patterns synchronize pan-Arctic glacier melt and permafrost thaw by Sasgen et al. 2024, Communications Earth and Environment, https://doi.org/10.1038/s43247-024-01548-8", https://doi.org/10.7910/DVN/XTETA5, Harvard Dataverse, V1 (2024).

Author contributions
I.S. designed the study and performed the research. I.S, G.S. and C.K. analysed and interpreted the data, H.M. and S.M. contributed CCI permafrost data output and assisted, together with G.G., in their analysis. G.S. and J.B. provided expertise on the field measurements. All authors contributed to the writing and editing of the paper.

Competing interests
The authors declare no competing interests.

Additional information
Supplementary information The online version contains supplementary material available at https://doi.org/10.1038/s43247-024-01548-8.

Correspondence and requests for materials should be addressed to Ingo Sasgen.

Peer review information *Communications Earth & Environment* thanks C. K. Shum and the other, anonymous, reviewer(s) for their contribution to the peer review of this work. Primary Handling Editor: Joe Aslin. A peer review file is available.

Reprints and permissions information is available at http://www.nature.com/reprints

Publisher's note Springer Nature remains neutral with regard to jurisdictional claims in published maps and institutional affiliations.